

1        **Sensitivity and Interpretation of Zonal Mean Climate from Two**  
2        **Atmospheric General Circulation Models with Different Dynamical**  
3        **Cores**

4  
5        He Zhang<sup>1\*</sup>, Minghua Zhang<sup>2</sup>, and Qingcun Zeng<sup>1</sup>

6  
7        1. ICCES, Institute of Atmospheric Physics, Chinese Academy of Sciences, Beijing,  
8        China

9        2. State University of New York at Stony Brook, Stony Brook, New York

10  
11  
12        Submit to **Monthly Weather Review**

13  
14  
15  
16  
17  
18  
19  
20  
21  

---

\* *Corresponding author address:* He Zhang, P.O. BOX 9804, ICCES, Institute of Atmospheric Physics, Chinese Academy of Sciences, Beijing 100029, China.  
E-mail: zhanghe@mail.iap.ac.cn

## Abstract

The dynamical cores of the fourth version of the Institute of Atmospheric Physics of Chinese Academy of Sciences atmospheric general circulation model (IAP AGCM4.0) and the Community Atmosphere Model (CAM3.1) are used with the same CAM3.1 physical parameterizations to study the sensitivity of the simulated time mean zonal mean climate. The IAP AGCM4.0 reduced the CAM3.1 warm bias in the troposphere from above 2K to less than 1 K. The IAP model also simulated weaker westerly jets that are more consistent with observations. However, when the two dynamical cores are used in the idealized Held-Suarez tests without moisture physics, the IAP AGCM core simulated a slight warmer troposphere than that in the CAM3.1. The causes of the differences in the full models and in the dry models are studied. We show that the relative warming center located near  $30^{\circ}$  in the IAP dynamical core is due to the downward motion forced by stronger eddies there. When moist physics is included, however, the diabatic heating becomes significant. The IAP model simulated reduced amount of high clouds thus less greenhouse effect of these clouds in the upper troposphere, leading to larger radiative cooling. The effect from the diabatic heating dominates the effect from the eddy-forced residual circulation. Therefore, the IAP model with full physics simulated a colder troposphere than the CAM3.1. Our results show how interactive physical processes can change the effect of a dynamical core on climate simulations.

## 1. Introduction

The IAP AGCM4.0 is the fourth version of the Institute of Atmospheric Physics (IAP) of Chinese Academy of Sciences atmospheric general circulation model developed by a model group in IAP. Its first version, IAP AGCM1.0, was designed in 1980's as the first general circulation model used for climate simulations in China (Zeng et al. 1989). IAP AGCM1.0 used a horizontal resolution of  $4^\circ$  latitude  $\times$   $5^\circ$  longitude and 2 layers in the vertical  $\sigma$  coordinate (Phillips 1957) with the top at 200 hPa. The second and third versions of the IAP AGCM used increased model resolutions of  $4^\circ\text{lat}\times 5^\circ\text{lon}\times 9\text{L}$  (9 levels) for IAP AGCM2.0 (Bi 1993; Liang 1996) and  $2^\circ\text{lat}\times 2.5^\circ\text{lon}\times 21\text{L}$  for IAP AGCM3.0 (Zuo 2003) respectively, along with modifications in the time integration scheme and physical parameterizations. These three versions of the IAP AGCM have been used to investigate the behavior of the earth's climate system and to predict summer precipitation anomalies and spring dust storms in China (e.g., Zeng et al. 1997; Xue et al. 2001; Chen et al. 2004). In the fourth version of the IAP AGCM, the main features of the dynamical core are inherited from the earlier versions, but new features have been introduced (details in section 2). The physical processes of the IAP AGCM4.0 however are not a simple inheritance of former versions. Instead, as an intermediate version, we adopted the full physics package of the Community Atmosphere Model version 3.1 (CAM3.1) (Collins et al. 2004). The model therefore gives us an opportunity to evaluate the impact of the IAP dynamical core on the simulated climate. New physical schemes of radiative transfer, heterogeneous cloud nucleation, convection parameterization, and a

new scheme for boundary layer fluxes are currently being introduced for the next version of the model.

The objective of this paper is to investigate the sensitivity of the IAP AGCM4.0 to the dynamical core. We show that the IAP model with full physics improved the temperature and zonal winds in the CAM3.1 by simulating a colder atmosphere, but the dry version of the model simulated a warmer climate than the CAM3.1. This type of opposite sensitivities of the moist and dry models to the dynamical core has been also reported in the past in other models (Chen et al. 1997), but the cause has not been explained before. Previous studies have also reported the impact of dynamical cores on atmospheric simulations (e.g., Boer and Denis 1997; Polvani et al. 2004; Jablonowski and Williamson 2006). To our knowledge, however, no study has investigated the different sensitivities between the dry and moist models.

This paper is organized as follows. Brief descriptions of the IAP AGCM4.0 and the experiments are given in section 2. Section 3 compares the simulations of temperature and general circulation between IAP AGCM4.0 and CAM3.1. Results from the dry model and aqua planet tests are also represented, along with diagnostics of eddy activities and interpretation in the transformed Eulerian mean framework. The last section contains a summary.

## **2. Model description and experimental setup**

### *a. IAP AGCM4.0*

The IAP AGCM4.0 is a finite-difference model with a terrain-following  $\sigma$

1 coordinate. A latitude-longitude grid with Arakawa's C grid staggering is used for the  
 2 horizontal discretization. In order to compare with CAM3.1 conveniently, the vertical  
 3 levels 26 and their locations are set approximately the same as CAM3.1 (about 2.2  
 4 hPa at top of the model). There are 128 grids in latitudes and 256 grids in longitudes,  
 5 which are also the same with the T85 spectral resolution of CAM3.1.

6 The model equations are based on the baroclinic primitive equations on sphere  
 7 by introducing the subtraction of standard stratification and the IAP transform.  
 8 Standard stratification is a "standard" static atmosphere characterized by state  
 9 variables  $\tilde{T}(p)$ ,  $\tilde{\phi}(p)$  and  $\tilde{p}_s(\theta, \lambda)$ , which satisfy the hydrostatic condition and the  
 10 standard earth's surface pressure as follows:

$$11 \quad \begin{cases} R\tilde{T}(p) = -p \frac{d\tilde{\phi}(p)}{dp} \\ \tilde{p}|_{z=\tilde{z}_s(\theta, \lambda)} \equiv \tilde{p}_s(\theta, \lambda) \end{cases} \quad (1)$$

12 where  $T$  is the temperature,  $\phi = gz$  is the geopotential,  $z$  the height,  $g$  the gravity  
 13 acceleration,  $p$  the pressure,  $p_s$  the surface pressure,  $\theta$  the co-latitude,  $\lambda$  the  
 14 longitude,  $\tilde{z}_s$  the elevation of earth's surface, and the superscript '~' denotes the  
 15 "standard atmosphere". By subtracting the "standard atmosphere" defined above, we  
 16 can get the perturbations (denoted by prime) as follows:

$$17 \quad \begin{cases} T'(\theta, \lambda, p, t) = T(\theta, \lambda, p, t) - \tilde{T}(p) \\ \phi'(\theta, \lambda, p, t) = \phi(\theta, \lambda, p, t) - \tilde{\phi}(p) \\ p'_{sa}(\theta, \lambda, t) = p_s(\theta, \lambda, t) - \tilde{p}_s(\theta, \lambda) \end{cases} \quad (2)$$

18 To obtain the concision form of the available energy conservation, we define the  
 19 following variable substitution, namely, the IAP transform:

$$\begin{cases} (U, V, \Phi) \equiv (Pu, Pv, PRT'/b) \\ P \equiv \sqrt{p_{es}/p_0}, \quad p_{es} = p_s - p_t \end{cases} \quad (3)$$

where  $p_t=2.2$  hPa is the pressure at the model top layer,  $p_0=1000$  hPa, and  $b=87.8$  m  $s^{-1}$  is the approximate value of  $\tilde{C}_0^2$ , which is the characteristic velocity of gravity-wave propagation of the standard atmosphere determined by  $\tilde{C}_0^2 = R(\kappa\tilde{T} - d\tilde{T}/d \ln p)$ , where  $\kappa = R/c_p$ ,  $R$  the gas constant for dry air, and  $c_p$  the specific heat of dry air at constant pressure.

After introducing the subtraction of standard stratification, the IAP transform, and the vertical coordinate transform  $\sigma \equiv (p - p_t)/p_{es}$ , the model equations ignored sinks and sources can be written as:

$$\begin{cases} \frac{\partial U}{\partial t} = -\sum_{m=1}^3 L_m(U) - P_\lambda - f^* V \\ \frac{\partial V}{\partial t} = -\sum_{m=1}^3 L_m(V) - P_\theta + f^* U \\ \frac{\partial \Phi}{\partial t} = -\sum_{m=1}^3 L_m(\Phi) + (1 - \delta_p) [\tilde{C}_0^2/b + \delta \cdot \kappa \Phi / P] (\Omega^{(1)} + \Omega^{(2)}) \\ \frac{\partial}{\partial t} \left( \frac{p'_{sa}}{p_0} \right) + D(P) + \frac{\partial P^2 \dot{\sigma}}{\partial \sigma} = \frac{1}{p_0} \nabla \cdot \left( \tilde{\rho}_{sa} k_{sa} \nabla \frac{p'_{sa}}{\tilde{\rho}_{sa}} \right) \end{cases} \quad (4)$$

where  $\delta_p \equiv p_t/p$ ,  $f^*$  is the Coriolis parameter determined by  $f^* = 2\Omega \cos \theta + u \text{ctg} \theta / a$  with  $a$  the earth radius,  $\Omega$  the angular velocity of the earth rotation,  $\tilde{\rho}_{sa} = \tilde{p}_s / R\tilde{T}_s$  is the density of the “standard atmosphere” at surface,  $k_{sa}$  is the dissipation coefficient,  $L_1$  and  $L_2$  are the horizontal advection operators and  $L_3$  is the vertical convection operator, which are defined by

$$\begin{cases}
L_1(F) \equiv \frac{1}{2a \sin \theta} \left( 2 \frac{\partial F u}{\partial \lambda} - F \frac{\partial u}{\partial \lambda} \right) \\
L_2(F) \equiv \frac{1}{2a \sin \theta} \left( 2 \frac{\partial F v \sin \theta}{\partial \theta} - F \frac{\partial v \sin \theta}{\partial \theta} \right) \\
L_3(F) \equiv \frac{1}{2} \left( 2 \frac{\partial F \dot{\sigma}}{\partial \sigma} - F \frac{\partial \dot{\sigma}}{\partial \sigma} \right)
\end{cases} \quad (5)$$

the gradient force terms are calculated according to the following formulas:

$$\begin{cases}
P_\lambda = P \frac{\partial \phi'}{a \sin \theta \partial \lambda} + \frac{b \Phi (1 - \delta_p)}{p_{es}} \cdot \frac{\partial p_{es}}{a \sin \theta \partial \lambda} \\
P_\theta = P \frac{\partial \phi'}{a \partial \theta} + \frac{b \Phi (1 - \delta_p)}{p_{es}} \cdot \frac{\partial p_{es}}{a \partial \theta}
\end{cases} \quad (6)$$

and other terms are determined by

$$\begin{cases}
\Omega^{(1)} \equiv \frac{P \dot{\sigma}}{\sigma} - \frac{1}{P} \left[ D(P) + \frac{\partial P^2 \dot{\sigma}}{\partial \sigma} \right] \\
\Omega^{(2)} \equiv \frac{U}{p_{es}} \cdot \frac{\partial p_{es}}{a \sin \theta \partial \lambda} + \frac{V}{p_{es}} \cdot \frac{\partial p_{es}}{a \partial \theta} \\
D(P) \equiv \frac{1}{a \sin \theta} \left( \frac{\partial P U}{\partial \lambda} + \frac{\partial P V \sin \theta}{\partial \theta} \right)
\end{cases} \quad (7)$$

It's worth noting that  $\delta$  in equations 4 is a “tracer” (should be 1 or 0). The case  $\delta = 0$ , is called as “standard stratification approximation” (SSA) proposed by Zeng et. al (1989). Previous study concluded that AAS a better approximation (Zhang 1990).

By introduction of the IAP transform, the kinetic energy  $E_k$ , the available potential energy  $E_{ep}$ , and the available surface potential energy  $E_{es}$  can be written as

$$\begin{cases}
E_k = \frac{P_0}{2g} \int_0^1 \int_0^{2\pi} \int_0^\pi (U^2 + V^2) a^2 \sin \theta d\theta d\lambda d\sigma \\
E_{ep} = \frac{P_0}{2g} \int_0^1 \int_0^{2\pi} \int_0^\pi \Phi^2 a^2 \sin \theta d\theta d\lambda d\sigma \\
E_{es} = \frac{1}{2g} \int_0^{2\pi} \int_0^\pi \frac{R \tilde{T}_s}{p_s} (p'_{sa})^2 a^2 \sin \theta d\theta d\lambda
\end{cases} \quad (8)$$

It can be proved that the equations (4) keep the total available energy conservation

1  $\frac{\partial}{\partial t}(E_k + E_{ep} + E_{es}) = 0$  under the standard stratification approximation:  $\delta = 0$ .

2 The central difference is used to discretize the terms on the right sides of  
 3 equations (4) with Arakawa's C grid. As well known, the zonal grid-sizes becomes  
 4 smaller and smaller when the latitudes close to the poles, which will produce the  
 5 computational unstabilities due to the high frequency effects. Two approaches are  
 6 applied in the model to alleviate this problem. One is the Fourier filtering poleward of  
 7  $70^\circ$  to damp the high frequency waves. Another is the so-called "flexible leaping-point  
 8 scheme", which enlarge the zonal grid-sizes at high latitudes. Take  $\partial F / \partial \lambda$  for  
 9 example, its discretization by "flexible leaping-point scheme" is

$$10 \left( \frac{\partial F}{\partial \lambda} \right)_i = \alpha_j \cdot \frac{F_{i+\frac{1}{2}} - F_{i-\frac{1}{2}}}{\Delta \lambda} + \beta_j \cdot \frac{F_{i+\frac{3}{2}} - F_{i-\frac{3}{2}}}{3\Delta \lambda}, \quad (9)$$

11 where the subscript  $i$  and  $j$  denote the  $i$ th and the  $j$ th grid points for longitudinal and  
 12 latitudinal direction respectively.  $\alpha_j$  and  $\beta_j$  are flexible coefficients depended on  
 13 latitudes and satisfy  $\alpha_j + \beta_j = 1$ .  $\beta_j$  increases linearly from 0 at  $30^\circ$  to 1 at  $70^\circ$ .

14 Furthermore, we split the model equations (4) to advection terms (e.g.  $\sum_{m=1}^3 L_m(U)$ ) with  
 15 time step 600s and advective terms (e.g.  $P_\lambda + f^*V$ ) with time step 200s to economize  
 16 CPU time without violating energy conservation.

17 The nonlinear iterative time integration method proposed by Zeng is used in the  
 18 model. For simplicity, the equation  $\frac{\partial F}{\partial t} + A(F) = 0$  is considered here, where  $A$  is a  
 19 nonlinear operator. The integration from time  $n$  to time  $n+1$  follows



$$\begin{aligned}
F_{(1)}^{n+1} - F^n &= \Delta t \cdot A \left( F^n \right) \\
F_{(2)}^{n+1} - F^n &= \Delta t \cdot A \left( F_{(1)}^{n+1} \right) \\
F_{(3)}^{n+1} - F^n &= \Delta t \cdot A \left( \frac{F_{(2)}^{n+1} + F^n}{2} \right) \\
&\vdots \\
F_{(2m)}^{n+1} - F^n &= \Delta t \cdot A \left( F_{(2m-1)}^{n+1} \right) \\
F_{(2m+1)}^{n+1} - F^n &= \Delta t \cdot A \left( \frac{F_{(2m)}^{n+1} + F^n}{2} \right)
\end{aligned} \tag{10}$$

where  $m=1, 2, 3, \dots$ . For current version of IAP AGCM, the iterative time is 3 ( $m=1$ ).

The horizontal diffusion is a  $\nabla^2$  form similar to Washington and Williamson (1977). The semi-Lagrangian method (Williamson and Rasch 1989) is used to solve water vapor forecast equations. As mentioned in the introduction, the CAM3.1 physical package (see Collins et al. 2004 in details) without any empirical physics parameters tuning is adopted in the current version IAP AGCM4.0. The time step for physics is 600s and the way the physics package coupled to the dynamics is process-split described by Williamson (2002).

#### *b. CAM3.1*

The CAM3.1 has three difference kinds of dynamical cores as well as different horizontal resolutions, and the standard Eulerian spectral-transform method with horizontal resolution T85 is used in this paper. The time step for dynamical core and physical package are both 600s, and the way the physics package coupled to the dynamics is process-split, which is the same with the IAP AGCM4.0. Other details about the CAM3.1 are given in Collins et al. (2004).

#### *c. experimental setup*

The IAP AGCM4.0 and CAM3.1 are both integrated for 17 years respectively

with nearly the same resolutions, the same physics package, the same boundary data and the same initial conditions. Averages of simulations in the last 15 years are presented. The SST and sea ice datasets used to force the AGCMs are climatological monthly datasets from blended products that combined the global Hadley Centre Sea Ice and Sea Surface Temperature (HadISST) dataset (Rayner et al. 2003) for years up to 1981 and the Smith/Reynolds EOF dataset (Reynolds et al. 2002) post-1981. The concentrations of greenhouse gases are held constant at their levels in 1990. The primary source of the validation data is NCEP/NCAR reanalysis (Kalnay et al. 1996). Both the model results and reanalysis data are truncated to T42 for direct comparison.

### 3. Results

#### *a. Temperature and general circulation from climate simulations*

We have examined a suite of atmospheric fields from the IAP AGCM4.0 by using the AMWG (Atmospheric Model Working Group) diagnostics package (Zhang 2009). The overall performance is similar to the CAM3.1 that was described in Hurrell et al. (2006). In this paper, therefore, we only focus on the differences between the simulations of the IAP AGCM4.0 and the CAM3.1.

Figures 1a and 1b show the deviation of the zonally averaged temperature from the NCEP reanalysis in the models. The differences between the IAP AGCM4.0 and the CAM3.1 15-year-mean simulations are shown in Figure 1c. As in most of the AGCMs (Boer et al. 1992), there exists a notable cold bias near the polar tropopause in both models. However, this cold bias in the IAP AGCM4.0 is about 2K smaller

1 than in the CAM3.1 in the Southern Hemisphere (SH). Moreover, the CAM3.1 has a  
2 warm bias throughout most of the troposphere. This warm bias is systematically  
3 reduced in the IAP AGCM4.0, especially in the tropical and subtropical regions  
4 between 30°N and 30°S, where the simulated temperature in the IAP AGCM4.0 is  
5 colder than that in the CAM3.1 by 1-2 K.

6       Distribution of zonal wind has traditionally been one of the fundamental  
7 measures of climate simulations. It is closely linked geostrophically to the  
8 temperature by thermal wind relation. Figures 2a to 2c show that both models  
9 simulated the main features of the observed zonal winds, including the westerly jet  
10 cores located near 200 hPa over the middle-latitudes of both hemispheres, and the  
11 tropical easterlies in the lower and middle troposphere as well as in the stratosphere.  
12 The two models all overestimated the intensity of the westerly jet in both hemispheres  
13 (Figures 2d and 2e). This overestimation however is reduced by about half in the IAP  
14 AGCM4.0 relative to the CAM3.1. The jets in the CAM3.1 are stronger than in the  
15 NCEP/NCAR reanalysis by 4-6 m s<sup>-1</sup> and 6-8 m s<sup>-1</sup> in Northern Hemisphere (NH) and  
16 SH respectively, while the corresponding biases in the IAP AGCM4.0 are about 2 m  
17 s<sup>-1</sup> and 4 m s<sup>-1</sup>. This can be more clearly seen in the difference figure between the two  
18 models (Figure 2f). Besides the strength, the locations of the jets are also different.  
19 The jet simulated in the IAP AGCM4.0 has a slight equatorward shift relative to that  
20 in the CAM3.1(Figures 2b and 2f), which may be mainly explained by the smaller  
21 meridional temperature gradient (Figure 1c) according to the thermal wind  
22 relationship. Furthermore, the relative heating above tropopause in tropical region

(Figure 1c) can also contribute the equatorward shift of the jet in the IAP AGCM4.0 (Lorenz and DeWeaver 2007).

Transports of heat and momentum by eddies are important mechanisms to establish the general circulation and maintain the energy balance as well as angular momentum conservation of the atmosphere. The observed climatological annual mean zonally averaged transient eddy heat fluxes in Figure 3c shows two peaks of poleward heat fluxes in the lower and upper troposphere at middle latitudes. Both simulations with the IAP AGCM4.0 (Figure 3a) and the CAM3.1 (Figure 3b) represent this two peaks pattern well, but seem too stronger than the observation due to the different way to calculate the eddies. The NCEP reanalysis annual mean transient eddy heat flux  $\overline{v'T'}$  is averaged from 12 monthly means, and 3-10 day filter is applied in every monthly mean. The simulated 15 years annual mean of  $\overline{v'T'}$  is calculated by

$$\overline{v'T'} = \overline{vT} - \overline{v}\overline{T} \quad (11)$$

where the bar denotes the 15 years annual mean and the prime denotes the deviation from the mean. Therefore, the value of  $v$  and  $T$  in every time step is implicit in the simulation calculations of  $\overline{v'T'}$  by (11), while only the daily data are used in the NCEP calculations. Consequently, the smaller samples and 3-10 day filter in the NCEP calculations lead the weaker amplitude of  $\overline{v'T'}$ .

More attentions should be taken to the differences of the two models in Figure 3d which indicates weaker poleward heat transport above 500 hPa, but a little stronger and equatorward shift of the transport below 700 hPa in the IAP AGCM4.0. The weaker poleward heat transport in the upper troposphere in the IAP model is the result

1 of weaker eddy activities. This can be seen in the eddy momentum transport of Figure  
 2 4. Previous studies have also shown large sensitivities of eddy kinetic energy to  
 3 dynamical cores (Wan et al. 2008). Therefore, the difference in the upper troposphere  
 4 can be attributed to the finite difference scheme that is more diffusive in the IAP  
 5 AGCM4.0 than in the CAM3.1 with the identical grid points. This conclusion is no  
 6 surprise since the spectral models represent a nominally higher resolution than grid  
 7 point models with the same number of grid points because of the very different  
 8 diffusive characteristics of grid-point models that need more resolution to resolve  
 9 sharp gradients (Williamson 2008). To compare reasonably, we also give the  
 10 differences from the simulations of the IAP AGCM4.0 with finer resolution  $1^\circ \times 1^\circ$  and  
 11 the CAM3.1 with T85 in Figure X. It can be seen that the eddy activities are also  
 12 weaker in the finer resolution IAP AGCM4.0 compared to the CAM3.1, although the  
 13 differences are reduced. The weaker eddy activities may be partly due to the more  
 14 damping horizontal diffusion scheme in the IAP AGCM4.0 than the CAM3.1 ( $\nabla^2$   
 15 versus  $\nabla^4$ ). Moreover, the difference in the lower troposphere in the heat transport,  
 16 as will be shown later, is likely related to the colder troposphere in the IAP model.

17

#### 18 *b. Held-Suarez test*

19 To understand the above differences between the two models, we carried out  
 20 idealized dry-model experiments proposed by Held and Suarez (1994), hereafter  
 21 referred to as H-S. Specified forcing is used in the thermodynamic and momentum  
 22 equations to yield a circulation that is grossly similar to the observation in the

1 troposphere. The thermal forcing is Newtonian relaxation to a specified temperature  
2 field of varying time scale with latitudes and pressure. The momentum forcing is a  
3 sink represented by Rayleigh friction in the lower troposphere. The atmosphere is  
4 integrated without moist processes, topography, land-sea contrast and seasonal or  
5 diurnal cycle.

6 The initial data is not important in the H-S test, since after a certain period of  
7 integration, the prescribed forcing drives the model dynamics to quasi-equilibrium  
8 state that is independent of the initial state. In this paper, the integration of the IAP  
9 AGCM4.0 dynamical core (hereafter IAP core) started from the same initial data as  
10 for the full model run. The CAM3.1 dynamical core (hereafter CAM core) was  
11 integrated from an earlier run of a lower resolution T42 to avoid the computational  
12 instability caused by disequilibrium between wind and pressure gradient due to lack  
13 of topography. As proposed by Held and Suarez (1994), both of the two models were  
14 integrated for 1200 days, and the time -mean fields and statistics are taken from the  
15 last 1000 days.

16 Figure 5 shows zonally averaged 1000-day mean temperature from the H-S tests  
17 with the IAP core and CAM core and their difference. The major feature of the real  
18 atmosphere is reproduced with the idealized forcing, although the simulated upper  
19 atmosphere is unrealistically cold by inactive forcing in the stratosphere. The  
20 simulated troposphere in the IAP core is **generally** warmer than that in the CAM core,  
21 which is opposite to the results found in the climate simulations, except in middle  
22 latitude below 700 hPa where the IAP core is 0.5-1.5K colder than the CAM core.

1 As expected from the thermal wind relationship, the simulated westerly jets in  
2 the IAP core are stronger than those from the CAM core (Figure 6). This difference is  
3 also opposite to that in the climate simulations, in which the jets are weaker in the IAP  
4 AGCM4.0.

5 The distribution of simulated eddy heat flux from H-S tests is presented in Figure  
6 7. The patterns of eddy heat fluxes of the H-S tests are similar to the climate  
7 simulations with two peaks located in lower and upper troposphere respectively. The  
8 differences between the two dynamical cores in Figure 7c are also similar to the  
9 climate simulations in Figure 3d with weaker heat transport in the upper peak and  
10 equatorward shift of the lower peak. The weaker poleward heat flux in the middle  
11 latitudes can explain why the tropospheric temperature from 30°S to 30°N is warmer  
12 in the IAP core in the H-S tests, and the equatorward shift of the heat flux in lower  
13 troposphere gives the probably reason for the cold there. The eddy momentum fluxes  
14 simulated by two cores are shown in Figure 8. Consistent with the full models, the  
15 values of the maximum are smaller in the IAP core. As will be shown later, these  
16 features of the differences between the two dynamical cores can be explained by the  
17 overall weaker wave activities in the IAP core.

### 18 19 *c. Aqua-planet test*

20 To understand why the IAP AGCM4.0 with full physics simulated a colder  
21 troposphere relative to CAM3.1, but a warmer troposphere in the H-S test, we further  
22 conducted aqua-planet experiments to examine the possible impact of the different

1 treatment of surface topography in the full models. Following Neale and Hoskins  
2 (2001), the full AGCM including dynamics and physics is used, but the surface  
3 boundary is drastically simplified by using a uniformly water-covered surface. The  
4 idealized control SST in Neale and Hoskins (2000) is used in this paper. The results  
5 from the aqua-planet tests by IAP AGCM4.0 (hereafter IAP aqua) and by CAM3.1  
6 (hereafter CAM aqua) are compared with the results from real climate simulations and  
7 from H-S tests. If the results are similar with that from H-S tests, the influence by  
8 topography will be the reason of the improvement of temperature simulation in IAP  
9 AGCM4.0. On the other hand, if the results are similar with that from real climate  
10 simulations, the contribution by topography is then not important.

11 As in Neale and Hoskins (2000), the aqua-planet simulations by the two models  
12 are integrated for 40 months, with the last 36 months used for the analysis. For  
13 simplicity, only the differences of the two models are given here (Figure 9). Relative  
14 to the CAM aqua, the following four features can be identified: (1) the IAP aqua  
15 simulated a colder troposphere on the aqua-planet (Figure 9a); (2) the westerly jet is  
16 weaker and displaced equatorward in the IAP model (Figure 9b); (3) the poleward  
17 eddy heat transport at middle latitude around 45°N and 45°S is weaker in the IAP  
18 aqua (Figure 9c); (4) the momentum transport is weaker in the IAP model (Figure 9d).  
19 The first two features are consistent with the differences between the two models with  
20 full physics, but opposite to those in the H-S tests. The last two features are consistent  
21 among all experiments.

22 These results confirm that the IAP dynamical core is more diffusive, with less



energetic eddies, and thus weaker poleward of heat. The cause of the difference in the temperature between the moist and dry models is therefore mostly related with the introduction of moist physics, which is further studied next.

#### *d. Residual circulation and diabatic heating*

Under steady-state conditions, the zonally averaged atmospheric thermodynamic balance is between the adiabatic cooling, the eddy forcing, and the diabatic heating.

As pointed out by Andrews and McIntyre (1976), there tends to be a strong cancellation between the convergence of eddy heat flux and the adiabatic cooling due to eddy-induced meridional circulation. Thus, it is the residual meridional circulation, after cancellation of these two terms that is more directly related to the diabatic heating. Using the transformed Eulerian mean (TEM) framework of Andrews and McIntyre (1976) **under quasi-geostrophic approximation, the meridional and vertical residual velocities** ( $\bar{v}^*$ ,  $\bar{w}^*$ ) and the vector Eliassen-Palm (EP) flux  $\mathbf{F}$  are defined by (see Holton 2004)

$$\bar{v}^* = \bar{v} - \frac{R}{\rho_0 H} \frac{\partial}{\partial z} \left( \frac{\rho_0}{N^2} \overline{v' T'} \right) \quad (12)$$

$$\bar{w}^* = \bar{w} + \frac{R}{H a \cos \varphi} \frac{\partial}{\partial \varphi} \left( \frac{\cos \varphi}{N^2} \overline{v' T'} \right) \quad (13)$$

$$\mathbf{F} = (F_\varphi, F_z) = \left( -\rho_0 a \cos \varphi \overline{v' u'}, \rho_0 a \cos \varphi \frac{R f}{H N^2} \overline{v' T'} \right) \quad (14)$$

the TEM thermodynamic equation can be written as

$$\frac{\partial \bar{T}}{\partial t} = \bar{Q} - \frac{H N^2}{R} \bar{w}^* \quad (15)$$

the residual circulation is related with eddy-forcing and diabatic heating as

$$\frac{\partial}{a^2 \partial \varphi} \left( \frac{1}{\cos \varphi} \frac{\partial \bar{\chi}^*}{\partial \varphi} \right) + \rho_0 \frac{f^2}{N^2} \frac{\partial}{\partial z} \left( \frac{1}{\rho_0 \cos \varphi} \frac{\partial \bar{\chi}^*}{\partial z} \right) = \frac{\rho_0}{N^2} \left[ \frac{\partial}{a \partial \varphi} \left( \frac{R \bar{Q}}{H} \right) + f \frac{\partial \bar{G}}{\partial z} \right] \quad (16)$$

with the stream function of the residual circulation ( $\bar{\chi}^*$ ) definition as

$$\rho_0 \bar{v}^* \cos \varphi = -\frac{\partial \bar{\chi}^*}{\partial z}, \quad \rho_0 \bar{w}^* \cos \varphi = \frac{\partial \bar{\chi}^*}{a \partial \varphi} \quad (17)$$

where

$$\bar{G} \equiv \frac{1}{\rho_0 a \cos \varphi} \nabla \cdot \mathbf{F} + \bar{X}$$

$$N^2 = \frac{R}{H} \left( \frac{\kappa \bar{T}}{H} + \frac{\partial \bar{T}}{\partial z} \right)$$

$$z = -H \ln \frac{p}{p_0}$$

$$\rho_0 = \frac{p_0}{gH} e^{-z/H}$$

In the above,  $\varphi$  is the latitude,  $f$  the Coriolis parameter,  $u$  the zonal wind,  $v$  the meridional wind,  $w$  the vertical velocity,  $T$  the temperature,  $X$  the subgrid-scale momentum forcing,  $Q$  the diabatic heating,  $N$  the buoyancy frequency,  $\rho_0$  the reference density, the scale height  $H = 7$  km, the reference pressure  $p_0 = 1000$  hPa, and other symbols are explained in section 2a. The bar denotes the zonal mean and the prime the deviation from the zonal mean. The EP flux is a measure of wave activities.

Figure 10a demonstrates the EP flux and its divergence in the IAP core. It can be seen that planetary waves propagate into the upper troposphere from the primary source region in the lower troposphere at middle latitudes. The difference field (Figure 10b) clearly shows that these wave activities in the IAP core are overall

weaker, except at low latitudes between 30°N and 30°S, where the EP flux is somewhat stronger in the IAP core.

Figure 11a gives the corresponding residual circulation from the IAP core. There is a broad descending motion, corresponding to adiabatic warming, in middle and high latitudes that balances the diabatic cooling from the temperature relaxation, in which the model temperature is larger than the reference temperature (not shown, see Figure 17 in Chen et al. 1997). In low latitudes, on the contrary, the residual circulation is ascent with a cooling effect, which balances the diabatic warming due to the colder simulated temperature compared to the reference temperature.

The difference field of the residual circulation from the two dry models shown in Figure 11b is significant below 500 hPa, with stronger upward motion in tropics and stronger downward flow near 30°N and 30°S. This stronger residual circulation equatorward of 30° in the IAP core is consistent with the stronger wave activities there. The stronger downward flow near 30° increases the adiabatic warming and therefore results in a warming larger than 0.5K there. Nevertheless, the stronger upward motion in tropics does not match the slight warmer tropical troposphere in Figure 5c. One possible reason is the relative stronger Newtonian relaxation (as diabatic heating  $\bar{Q}$  in equation 15) cancels the adiabatic cooling. Furthermore, the quasi-geostrophic approximation has relative large errors in the tropics. Figure 11b also indicates the upward motion differences around 40°N and 40°S. This explains the colder temperature difference in Figure 5c.

This interpretation becomes different for the moist models. Figure 10d shows the

1 difference of EP fluxes as a measure of the wave activities between the two moist  
2 models. The IAP model also simulated overall weaker wave activities throughout the  
3 troposphere. The change in the residual circulation in Figure 11d is however very  
4 different. In each hemisphere, the circulation is weaker in low latitudes, but stronger  
5 in middle latitudes. This lack of direct correspondence between the eddy activity and  
6 residual circulation suggests that the diabatic heating also played a major role, as  
7 discussed below.

8

9 *e. Interaction between moist physics and dynamics*

10 Equation (4) shows that under steady state conditions, the adiabatic cooling from  
11 the residual circulation should balance the diabatic heating. However, the interaction  
12 between the adiabatic cooling and the diabatic heating in dry models is different from  
13 that in moist models. In the dry models, the diabatic heating term is the relaxation to  
14 temperature, so it is passive to adiabatic cooling. While in the moist models, the  
15 interaction between diabatic heating and adiabatic cooling is so strong that we can't  
16 tell which is active and which is passive. The above conclusions can be demonstrated  
17 from Figure 12, which gives the evolution of adiabatic heating rate, diabatic heating  
18 rate and total heating rate in H-S tests with IAP dry model as well as in climate  
19 simulations with IAP moist model, respectively. The corresponding correlation  
20 coefficients of adiabatic heating, diabatic heating and total heating are given in Table  
21 1. In H-S test, there is no significant correlation between adiabatic heating and  
22 diabatic heating, and the total heating primarily follows on the adiabatic heating term.

1 However, in the moist model, there is significant negative correlation between  
2 adiabatic heating and diabatic heating. Namely, if there is a warming due to adiabatic  
3 processes, the diabatic processes will make a quick response to cool the atmosphere.  
4 Both of adiabatic heating and diabatic heating have a significant contribution to the  
5 total heating.

6 The major diabatic heating considered in AGCMs includes radiative heating,  
7 vertical diffusive heating and the heating due to moist processes, such as convection.  
8 Because the vertical diffusive heating merely affects low troposphere below 850 hPa,  
9 we will not discuss it here since we focus on vertical distribution of temperature at  
10 middle and high troposphere. Figure 13 shows the radiative heating in the IAP and  
11 CAM models with full physics and their difference. It is seen that the IAP model has  
12 larger radiative cooling in the troposphere from 700 hPa to 300 hPa, with the pattern  
13 of difference in Figure 13c to be similar to the pattern of temperature difference in  
14 Figure 1c. This suggests that the different radiative cooling may be the major reason for  
15 different simulated temperature in the two moist models.

16 The variables that we used to calculate the radiative heating include temperature,  
17 clouds and water vapor. To investigate which of the variables is dominant to cause the  
18 different radiative cooling between the two models, we carried out a series of offline  
19 radiation calculations. The set of calculations is listed in Table 2. For simplicity, we  
20 used the annual mean from climate simulation from the two moist models in the  
21 offline calculations. Figure 14a gives radiative heating difference between the  
22 IAP\_ctrl and the CAM\_ctrl. There is a larger radiative cooling in most region of

1 troposphere in IAP moist model compared to CAM moist model. The pattern of this  
2 cooling area is qualitatively the same as that in Figure 13c; the exact agreement is not  
3 expected since only annual mean fields are used. Figure 14b shows the difference of  
4 heating rate due to change of clouds. It is seen that cloud fraction is the dominant  
5 contributor to the different radiative cooling between the two moist models, while  
6 temperature and water vapor have much smaller contributions (Fig. 14c, d). The cloud  
7 fractions in the two moist models and their differences are given in Figure 15. The  
8 IAP model simulated less high clouds (Figure 15c), and thus less greenhouse effect of  
9 clouds (Figure 14b) in the upper troposphere, leading to larger radiative cooling and  
10 colder troposphere. The cause of the smaller cloud amount in the upper troposphere is  
11 presumably due to the less energetic eddy activities, but the interactions are  
12 complicated and need further study.

13

#### 14 **4. Summary**

15 The zonal mean temperature, zonal wind and eddy fluxes with the IAP  
16 AGCM4.0 and CAM3.1 are evaluated against the NCEP reanalysis data. The results  
17 reveal that the tropical tropospheric temperature in the IAP AGCM4.0 simulation is  
18 colder than that in the CAM3.1, but closer to NCEP reanalysis. The model also  
19 simulated a better distribution of the westerly jets. Since the main difference of the  
20 two models is the dynamical core, we used the idealized H-S test to investigate the  
21 direct impact of the dynamical cores. We showed that the IAP AGCM4.0 simulated a  
22 warmer troposphere in H-S test than the CAM3.1, which is nearly opposite to that in

1 the full model. We carried out aqua-planet experiments to rule out the impact of  
2 different treatment of topography as the cause of the difference in the full models.

3 We used transformed Eulerian mean diagnostics to show that wave activities are  
4 weaker in the IAP AGCM4.0 at middle and high latitudes regardless of whether  
5 moisture physics is included or not, a consequence of the more damping horizontal  
6 diffusion scheme and less energetic eddies. In the dry model, the stronger eddies  
7 forced a stronger downward motion near  $30^\circ$  in each hemisphere that can explain the  
8 warming larger than 0.5K in the IAP model. In tropical troposphere, the temperature  
9 difference between the two models is too small, which might be caused by the  
10 cancellation between the residual circulation and the Newtonian relaxation. In the  
11 moist model, however, the residual circulation is in balance with the diabatic heating  
12 from physical parameterizations. There is larger radiative cooling in the IAP model,  
13 owing to smaller cloud amount in the upper troposphere and weaker greenhouse  
14 effects of clouds. This explains the colder troposphere in the IAP model with full  
15 physics than that in the CAM model.

16 Our study demonstrates how interactive moist physics, especially clouds, can  
17 change the behavior of a dynamical core in climate models. It points to the need to  
18 understand dynamical cores both in isolation and with full physics. To our knowledge,  
19 this is the first effort to report and analyze the cause of the opposite impact of  
20 dynamical core between dry and moist models on climate simulation. Future research  
21 will focus on the impact of dynamical core on high latitude and stratospheric climate,  
22 and on the mechanism of cloud responses.

1  
2  
3  
4  
5  
6  
7  
8  
9  
10  
11  
12  
13  
14  
15  
16  
17  
18  
19  
20  
21  
22

**Acknowledgments.** We wish to thank Dr. Wuyin Lin for his help and discussion in the course of this study. This research was supported by National Basic Research Program of China (973 Program) under Grant Nos. 2010CB951901 as well as the National Natural Science Foundation of China under Grant Nos. 41005054 and 40830103. Additional support is from the Climate Change and Prediction Program of the US Department of Energy, and the Modeling and Analysis Program of the National Administration for Space Studies to the Stony Brook University. Part of this research was carried out while the first author visited the Institute for Terrestrial and Planetary Atmosphere of the Stony brook University.



1   **References:**

- 2   Andrews, D. G., and McIntyre, 1976: Planetary waves in horizontal and vertical shear:  
3       The generalized Eliassen-Palm relation and the mean zonal acceleration. *J. Atmos.*  
4       *Sci.*, **33**, 2031-2048.
- 5   Bi, X., 1993: IAP 9L AGCM and climate simulation. Ph. D. dissertation (in Chinese),  
6       Institute of Atmospheric Physics, Chinese Academy of Sciences, 210 pp.
- 7   Boer, G. J., and coauthors, 1992: Some results from an intercomparison of the  
8       climates simulated by 14 atmospheric general circulation models. *J. Geophys. Res.*,  
9       **97**, 12771–12786.
- 10   Boer, G. J., and B. Denis, 1997: Numerical convergence of the dynamics of a GCM.  
11       *Climate. Dyn.*, **13**, 359-374.
- 12   Chen, H., Z. Lin, and G. Zhou, 2004: Experimental dynamical prediction of spring  
13       dust storm events in China. *Climatic and Environmental Research* (in Chinese), **9**,  
14       182-190.
- 15   Chen, M., R. B. Rood, and L. L. Takacs, 1997: Impact of a semi-Lagrangian and an  
16       Eulerian dynamical core on climate simulation. *J. Climate*, **10**, 2374-2389.
- 17   Collins, W. D., and coauthors, 2004: Description of the NCAR **Community**  
18       **Atmosphere Model** (CAM3.0). NCAR Technical Note NCAR/TN-464+STR,  
19       xii+214 pp.
- 20   Held, I. M., and M. J. Suarez, 1994: A proposal for the intercomparison of the  
21       dynamical cores of atmospheric general circulation models. *Bull. Amer. Meteor.*  
22       *Soc.*, **75**, 1825-1830.

1 Holton, J. R., 2004: An introduction to dynamic meteorology. International  
2 Geophysical Series, Vol. 88, 4 ed., Academic Press, 535 pp.

3 Hurrell, J. W., J. J. Hack, A. S. Phillips, J. Caron, and J. Yin, 2006: The dynamical  
4 simulation of the **Community Atmosphere Model** version 3 (CAM3). *J. Climate*,  
5 **19**, 2162-2183.

6 Jablonowski, C., and D. L. Williamson, 2006: Baroclinic wave test case for Dynamical  
7 cores of GCMs. *Quart. J. Roy. Meteor. Soc.*, **132**, 2943-2976.

8 Kalnay, E., and coauthors, 1996: The NCEP/NCAR 40-year reanalysis project. *Bull.*  
9 *Amer. Meteor. Soc.*, **77**, 437-471.

10 Liang, X., 1996: Description of a nine-level grid point atmospheric general circulation  
11 model. *Adv. Atmos. Sci.*, **13**, 269-298.

12 Lin, Z., and Q. Zeng, 1997: Simulation of East Asian summer monsoon by using an  
13 improved AGCM. *Adv. Atmos. Sci.*, **14**, 513-526.

14 Lorenz, D. J., and E. T. DeWeaver, 2007: Tropopause height and zonal wind response  
15 to global warming in the IPCC scenario integrations, *J. Geophys. Res.*, **112**,  
16 D10119, doi:10.1029/2006JD008087.

17 Neale, R. B., and B. J. Hoskins, 2000: A standard test for AGCMs including their  
18 physical parameterizations: I: The proposal. *Atmos. Sci. Lett.*, **1**, 101-107.

19 **Phillips, N. A., 1957: A coordinate system having some special advantages for**  
20 **numerical forecasting. *J. Meteor.*, **14**, 184–185.**

21 Polvani, L. M., R. K. Scott, and S. J. Thomas, 2004: Numerically converged solutions  
22 of the global primitive equations for testing the dynamical core of atmospheric

1 GCMs. *Mon. Wea. Rev.*, **132**, 2539-2552.

2 Rayner, N. A., and coauthors, 2003: Global analyses of sea surface temperature, sea  
3 ice, and night marine air temperature since the late nineteenth century. *J. Geophys.*  
4 *Res.*, **108**, 4407, doi:10.1029/2002JD002670.

5 Reynolds, R. W., N. A. Rayner, T. M. Smith, D. C. Stokes, and W. Wang, 2002: An  
6 improved in situ and satellite SST analysis for climate. *J. Climate*, **15**, 1609-1625.

7 Xue, F., X. Bi, and Y. Lin, 2001: Modelling the global monsoon system by IAP 9L  
8 AGCM. *Adv. Atmos. Sci.*, **18**, 404-412.

9 Wan, H., M. A. Giorgetta, and B. Luca, 2008: Ensemble Held-Suarez test with a  
10 spectral transform model: variability, sensitivity, and convergence. *Mon. Wea. Rev.*,  
11 **136**, 1075-1092.

12 Washington, W. M., and D. L. Williamson, 1977: A description of the NCAR global  
13 circulation models. *Methods in Computational Physics*, **17**, 111-173.

14 Williamson, D. L., and P. J. Rasch, 1989: Two-dimensional semi-Lagrangian transport  
15 with shap-preserving interpolation. *Mon. Wea. Rev.*, **117**: 102-129.

16 Williamson, D. L., 2002: Time-split versus process-split coupling of  
17 parameterizations and dynamical core. *Mon. Wea. Rev.*, **130**: 2024-2041.

18 Williamson, D. L., 2008: Equivalent finite volume and Eulerian spectral transform  
19 horizontal resolutions established from aqua-planet simulations. *Tellus*, **60A**,  
20 839-847.

21 Zeng, Q., and coauthors, 1989: Documentation of IAP Two-Level Atmospheric  
22 General Circulation Model. DOE/ER/60314-H1, TR044. 383 pp.

1 Zeng, Q., and coauthors, 1997: Seasonal and extraseasonal predictions of summer  
2 monsoon precipitation by GCMs. *Adv. Atmos. Sci.*, **14**, 163-176.

3 Zeng, Q., and M. Mu, 2002: The design of compact and internally consistent model of  
4 climate system dynamics. *Chinese J. Atmos. Sci.*, **26**: 107-113.

5 Zhang, H., 2009: Development of IAP atmospheric general circulation model version  
6 4.0 and its climate simulations. Ph. D. dissertation (in Chinese), Institute of  
7 Atmospheric Physics, Chinese Academy of Sciences, 194 pp.

8 Zhang, H., Z. Lin, and Q. Zeng, 2009: The computational scheme and the test for  
9 dynamical framework of IAP AGCM-4. *Chinese J. Atmos. Sci.* (in Chinese), **33**,  
10 1267-1285.

11 Zhang, X., 1990: Dynamical framework of IAP nine-level atmospheric general  
12 circulation model. *Adv. Atmos. Sci.*, **7**, 67-77.

13 Zuo, R., 2003: Development of new generation grid point atmospheric general  
14 circulation model with high resolution. Ph. D. dissertation (in Chinese), China  
15 People's Liberation Army University of Science and Technology, 328 pp.

**Table 1.** Correlation coefficients of adiabatic heating, diabatic heating and total heating in climate simulation and H-S test by the IAP model.

	correlation coefficients		
	adiabatic heating	diabatic heating	adiabatic heating
	.vs. total heating	.vs. total heating	.vs. diabatic heating
climate simulation	0.445	0.443	-0.603
H-S test	0.906	0.123	-0.309

1 **Table 2.** Design of offline radiation calculations, the fields with suffix ‘CAM’ are  
2 from climate simulation of CAM, while the fields with suffix ‘IAP’ are from climate  
3 simulation of IAP

Experiment Name	Sensitive Fields		
	Temperature	Specific Humidity	Cloud Fraction
CAM_ctrl	T_CAM	Q_CAM	CLD_CAM
IAP_ctrl	T_IAP	Q_IAP	CLD_IAP
IAP_CLDonly	T_CAM	Q_CAM	CLD_IAP
IAP_Tonly	T_IAP	Q_CAM	CLD_CAM
IAP_Qonly	T_CAM	Q_IAP	CLD_CAM

## Figure Captions

**Fig.1.** The biases of zonally averaged 15-year annual mean temperature from (a) IAP and (b) CAM simulations with contrast to NCEP reanalysis data, and (c) their difference (IAP - CAM). Contour intervals are 1 K in (a) and (b) and 0.5 K in (c), and negative values are shaded.

**Fig. 2.** Zonally averaged 15-year annual mean zonal wind from (a) IAP , (b) CAM, (c) NCEP reanalysis data, the biases of (d) IAP and (e) CAM with contrast to NCEP reanalysis data, and (f) the difference of the two simulations (IAP - CAM). Contour intervals are 5 m s<sup>-1</sup> in (a), (b) and (c), 2 m s<sup>-1</sup> in (d) and (e), and 1 m s<sup>-1</sup> in (f). Negative values are shaded.

**Fig. 3.** Zonally averaged 15-year annual mean transient eddy heat flux from (a) IAP, (b) CAM, (c) NCEP reanalysis data, and (d) the difference of the two simulations (IAP - CAM). Contour intervals are 3 K m s<sup>-1</sup> in (a) and (b), 1 K m s<sup>-1</sup> in (c) and (d), and negative values are shaded.

**Fig. 4.** Same as Fig. 3, but for transient eddy momentum flux. Contour intervals are 10 m<sup>2</sup> s<sup>-2</sup> in (a) and (b), and 4 m<sup>2</sup> s<sup>-2</sup> in (c) and (d).

**Fig. 5.** Zonally averaged 1000-day mean temperature from the Held-Suarez tests with the (a) IAP and (b) CAM dynamical cores, and (c) their difference (IAP - CAM).

1 Contour intervals are 5 K in (a) and (b), 0.5 K in (c) and negative values are shaded.

2 **Fig. 6.** Same as Fig. 5, but for zonal wind. Contour intervals are 5 m s<sup>-1</sup> in (a) and (b),  
3 and 1 m s<sup>-1</sup> in (c).

4

5 **Fig. 7.** Same as Fig. 5, but for transient eddy heat flux. Contour intervals are 3 K m s<sup>-1</sup>  
6 in (a) and (b), and 1 K m s<sup>-1</sup> in (c).

7

8 **Fig. 8.** Same as Fig. 5, but for transient eddy momentum flux. Contour intervals are  
9 10 m<sup>2</sup> s<sup>-2</sup> in (a) and (b), and 2 m<sup>2</sup> s<sup>-2</sup> in (c).

10

11 **Fig. 9.** The difference of zonally averaged annual mean between IAP and CAM from  
12 aqua planet tests: (a) temperature; (b) zonal wind; (c) transient eddy heat flux; (d)  
13 transient eddy momentum flux. Contour intervals are 0.5 K in (a), 2 m s<sup>-1</sup> in (b), 1 K  
14 m s<sup>-1</sup> in (c), 3 m<sup>2</sup> s<sup>-2</sup> in (d), and negative values are shaded.

15

16 **Fig. 10.** Vector EP flux and its divergence from the Held-Suarez tests with the (a) IAP  
17 and (b) differences between IAP and CAM dynamical cores (IAP - CAM), and from  
18 climate simulations from (c) IAP AGCM4.0 and (d) differences between IAP  
19 AGCM4.0 and CAM3.1 (IAP AGCM4.0 – CAM3.1). Contour intervals are 2 m s<sup>-1</sup>  
20 day<sup>-1</sup> in (a) and (c), and 1 m s<sup>-1</sup> day<sup>-1</sup> in (b) and (d). The flux is in the unit of kg s<sup>-2</sup>.  
21 The vertical component of the flux is multiplied by a factor of 100 to make proper  
22 vector plots.



1

2 **Fig. 11.** Same as Fig. 10, but for meridional stream function of residual circulation.  
3 Contour intervals are  $3 \times 10^2 \text{ kg m}^{-1} \text{ s}^{-1}$  in (a) and (c), and  $1 \times 10^2 \text{ kg m}^{-1} \text{ s}^{-1}$  in (b) and (d)  
4 and negative values are shaded.

5

6 **Fig. 12.** Evolution of heating rate from the IAP model in (a) Held-Suarez test and (b)  
7 climate simulation in troposphere (150 hPa – 1000 hPa) at low latitude (30°S - 30°N).  
8 Solid square: diabatic heating rate, solid triangle: adiabatic heating rate, hollow circle:  
9 total heating rate. Unit:  $10^{-6} \text{ K s}^{-1}$

10

11 **Fig. 13.** Zonally averaged annual mean radiative diabatic heating rate from (a) IAP  
12 and (b) CAM simulations, and (c) their difference (IAP - CAM). Contour intervals are  
13  $0.4 \text{ K day}^{-1}$  in (a) and (b),  $0.1 \text{ K day}^{-1}$  in (c) and negative values are shaded.

14

15 **Fig. 14.** Differences of radiative diabatic heating rate from the sensitive experiments:  
16 (a) IAP\_ctrl - CAM\_ctrl, (b) IAP\_CLDonly - CAM\_ctrl, (c) IAP\_Tonly - CAM\_ctrl,  
17 (d) IAP\_Qonly - CAM\_ctrl. Contour intervals are  $0.2 \text{ K day}^{-1}$  in (a) and (b),  $0.05 \text{ K}$   
18  $\text{day}^{-1}$  in (c) and (d), and negative values are shaded.

19

20 **Fig. 15.** Cloud fraction used in experiment (a) IAP\_CLDonly and (b) CAM\_ctrl, and  
21 (c) their difference (IAP\_CLDonly - CAM\_ctrl). Contour values are 0.05 in (a) and  
22 (b), 0.02 in (c) and negative values are shaded.

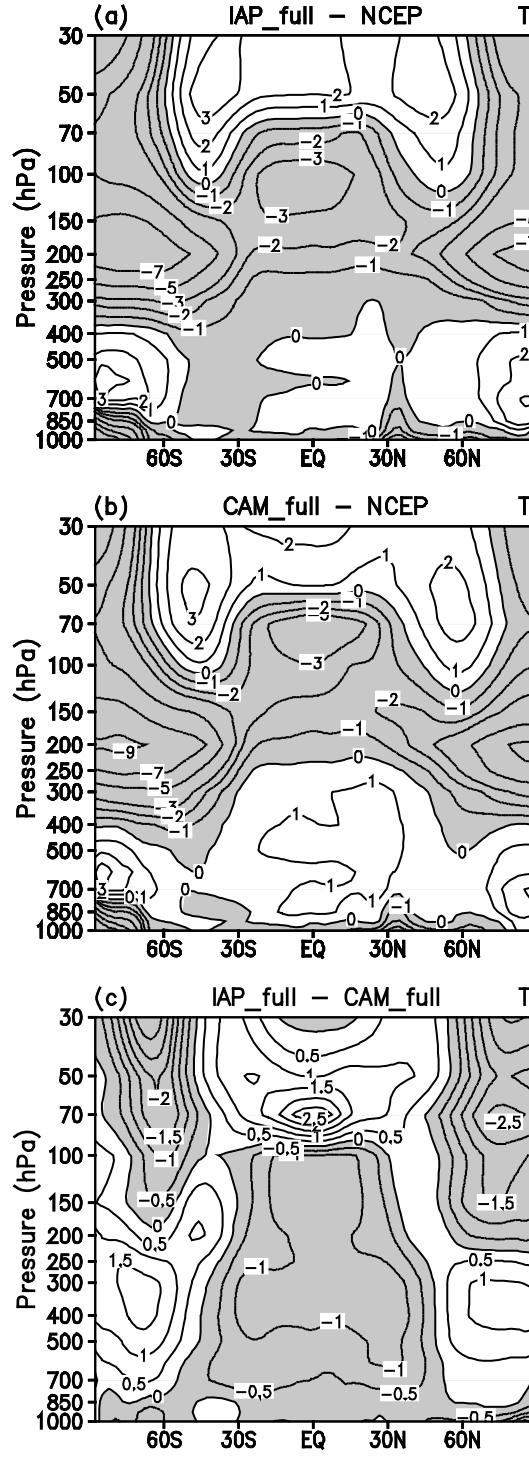


Fig.1. The biases of zonally averaged 15-year annual mean temperature from (a) IAP and (b) CAM simulations with contrast to NCEP reanalysis data, and (c) their difference (IAP - CAM). Contour intervals are 1 K in (a) and (b) and 0.5 K in (c), and negative values are shaded.

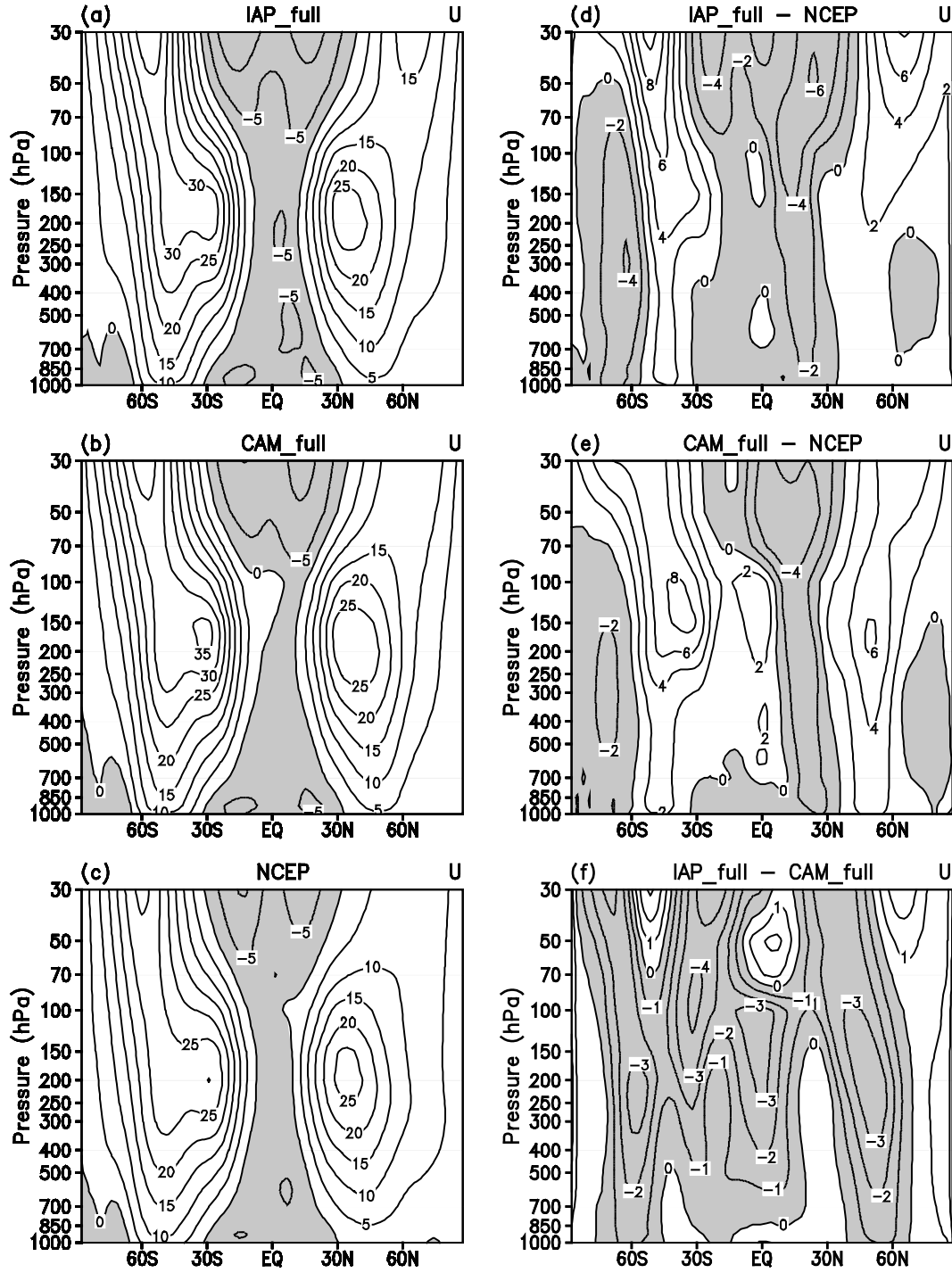


Fig. 2. Zonally averaged 15-year annual mean zonal wind from (a) IAP, (b) CAM, (c) NCEP reanalysis data, the biases of (d) IAP and (e) CAM with contrast to NCEP reanalysis data, and (f) the difference of the two simulations (IAP - CAM). Contour intervals are 5 m s<sup>-1</sup> in (a), (b) and (c), 2 m s<sup>-1</sup> in (d) and (e), and 1 m s<sup>-1</sup> in (f).

Negative values are shaded.

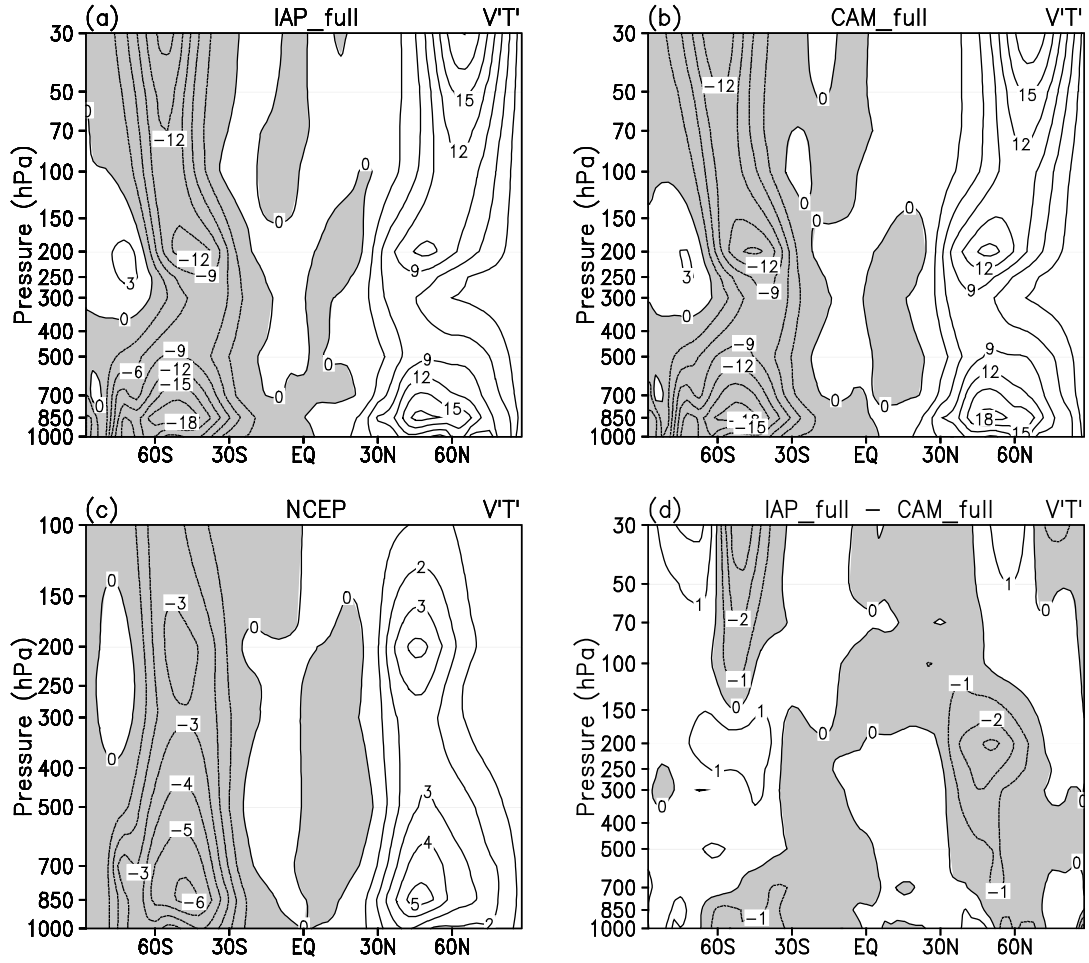


Fig. 3. Zonally averaged **15-year** annual mean transient eddy heat flux from (a) IAP, (b) CAM, (c) NCEP reanalysis data, and (d) the difference of the two simulations (IAP - CAM). Contour intervals are 3 K m s<sup>-1</sup> in (a) and (b), 1 K m s<sup>-1</sup> in (c) and (d), and negative values are shaded.

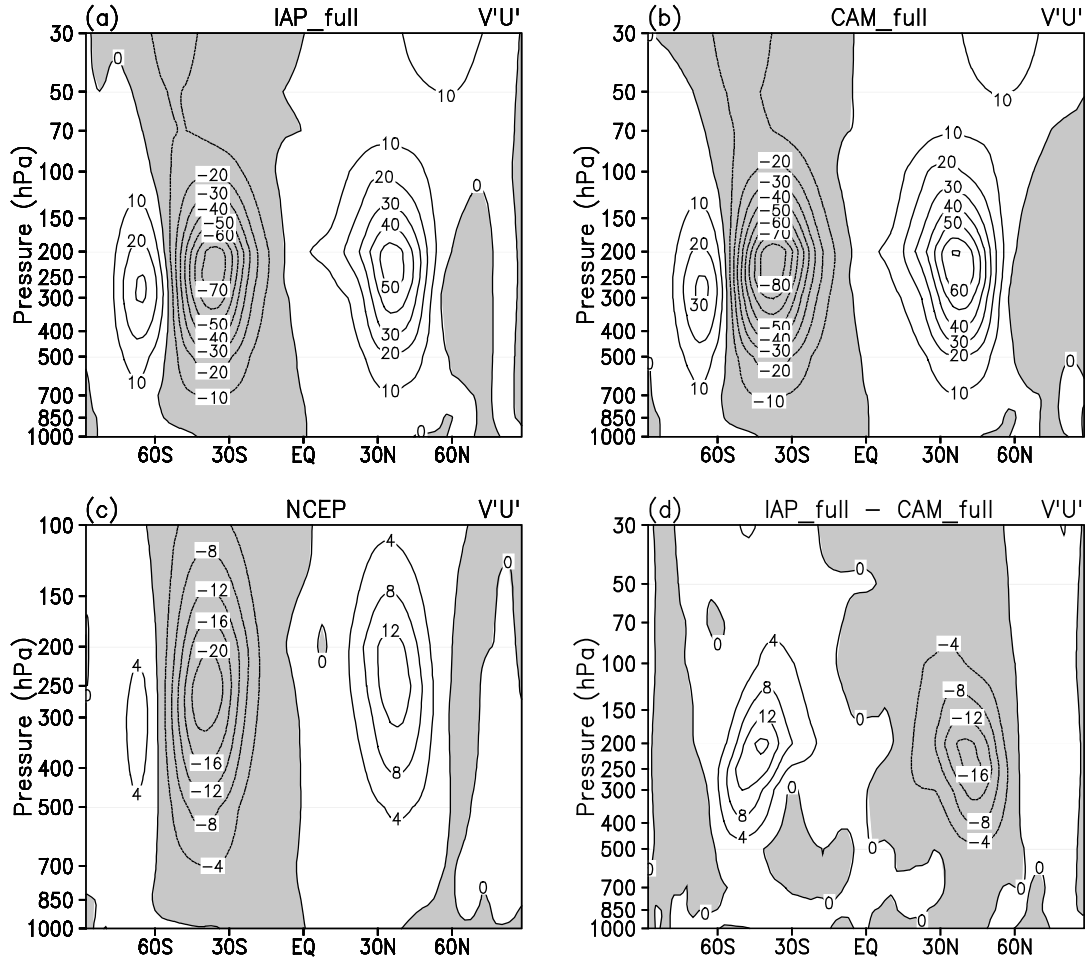


Fig. 4. Same as Fig. 3, but for transient eddy momentum flux. Contour intervals are  $10 \text{ m}^2 \text{s}^{-2}$  in (a) and (b), and  $4 \text{ m}^2 \text{s}^{-2}$  in (c) and (d).

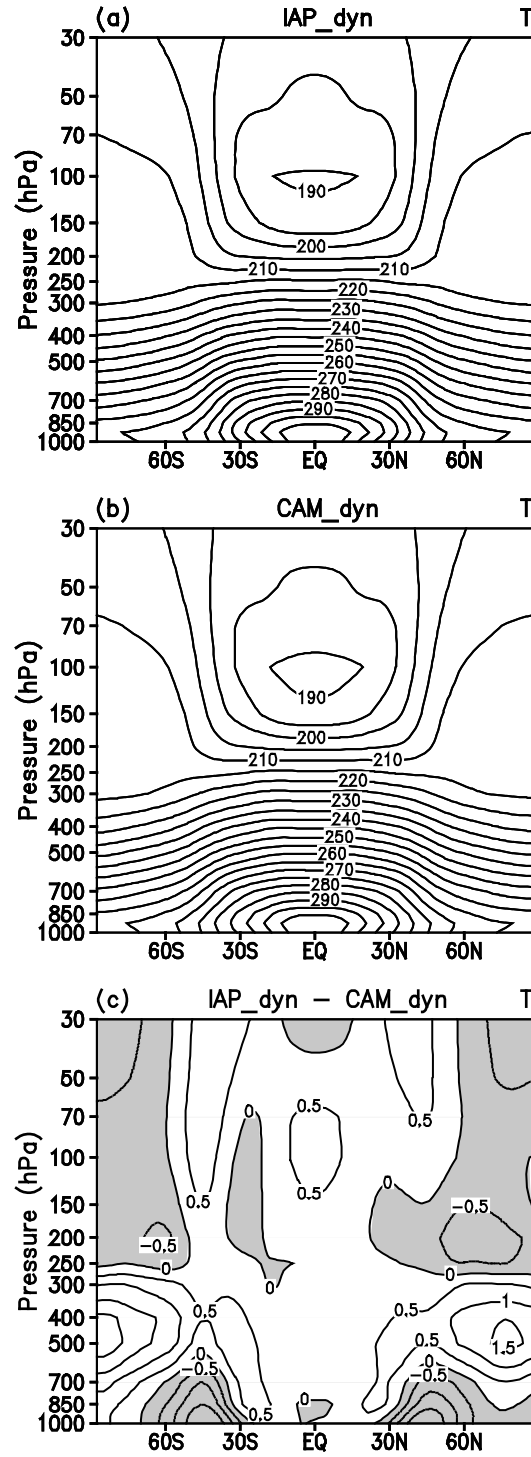


Fig. 5. Zonally averaged 1000-day mean temperature from the Held-Suarez tests with the (a) IAP and (b) CAM dynamical cores, and (c) their difference (IAP - CAM). Contour intervals are 5 K in (a) and (b), 0.5 K in (c) and negative values are shaded.

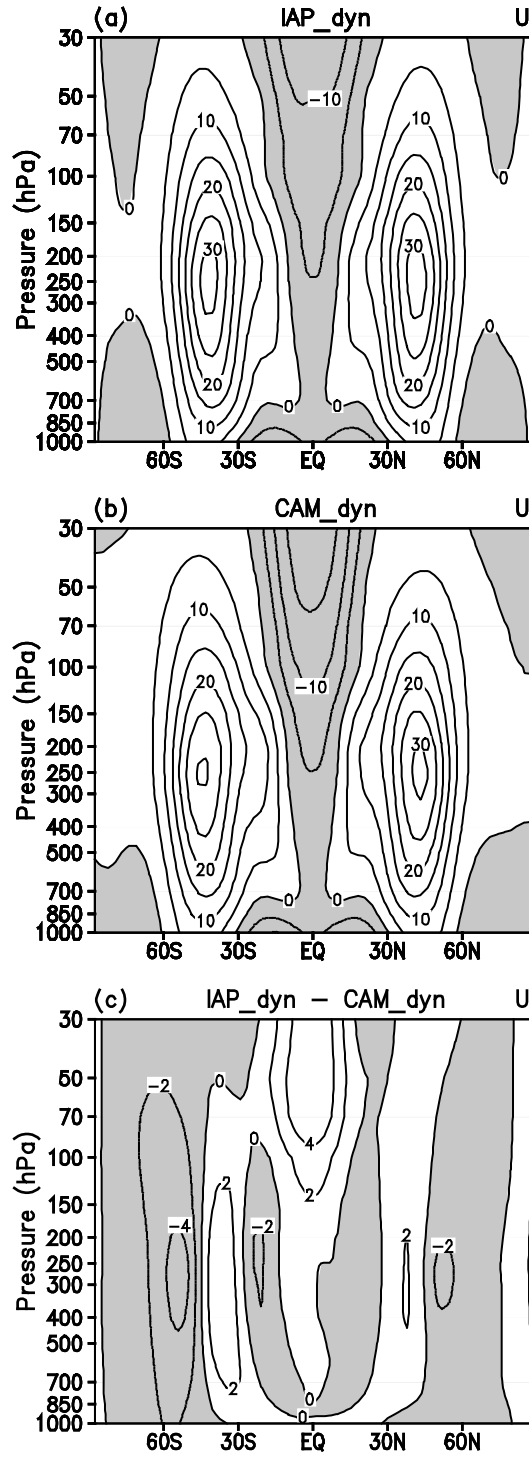


Fig. 6. Same as Fig. 5, but for zonal wind. Contour intervals are  $5 \text{ m s}^{-1}$  in (a) and (b), and  $2 \text{ m s}^{-1}$  in (c).

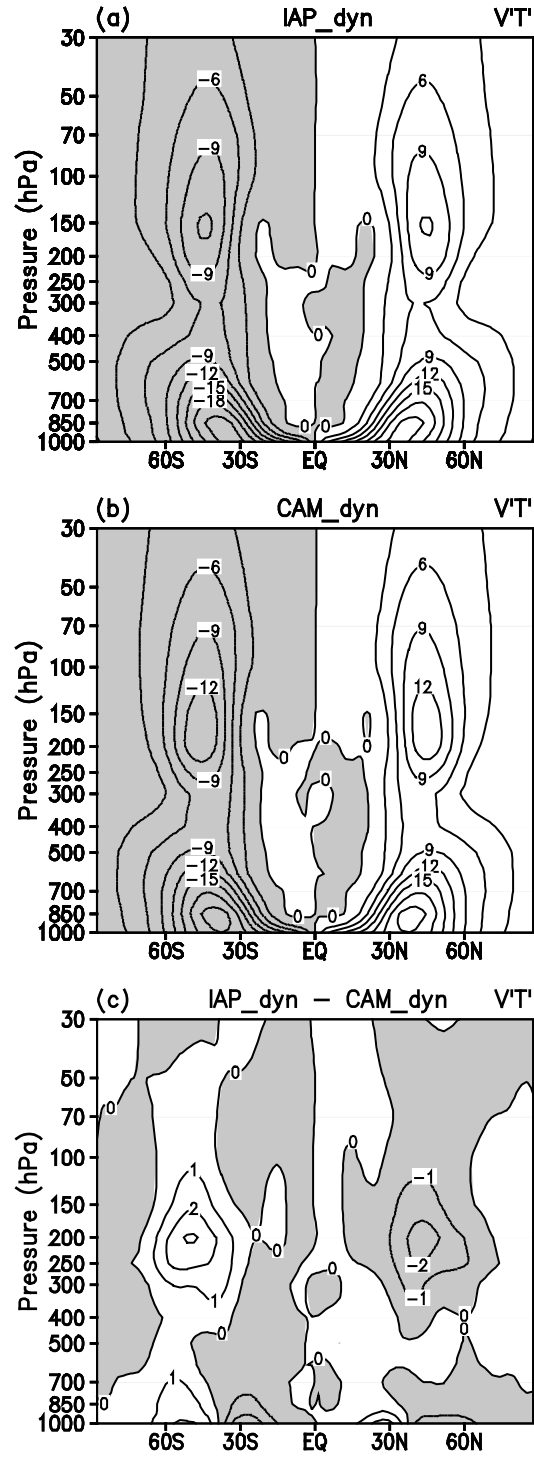


Fig. 7. Same as Fig. 5, but for transient eddy heat flux. Contour intervals are  $3 \text{ K m s}^{-1}$  in (a) and (b), and  $1 \text{ K m s}^{-1}$  in (c).



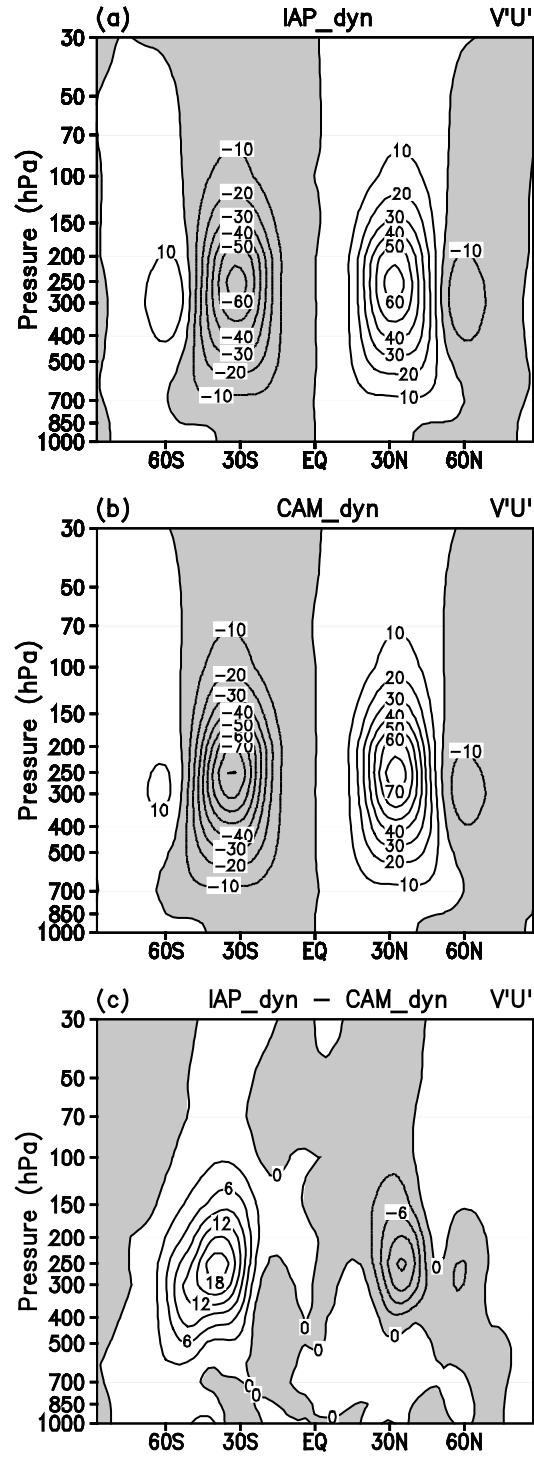


Fig. 8. Same as Fig. 5, but for transient eddy momentum flux. Contour intervals are  $10 \text{ m}^2 \text{s}^{-2}$  in (a) and (b), and  $3 \text{ m}^2 \text{s}^{-2}$  in (c).

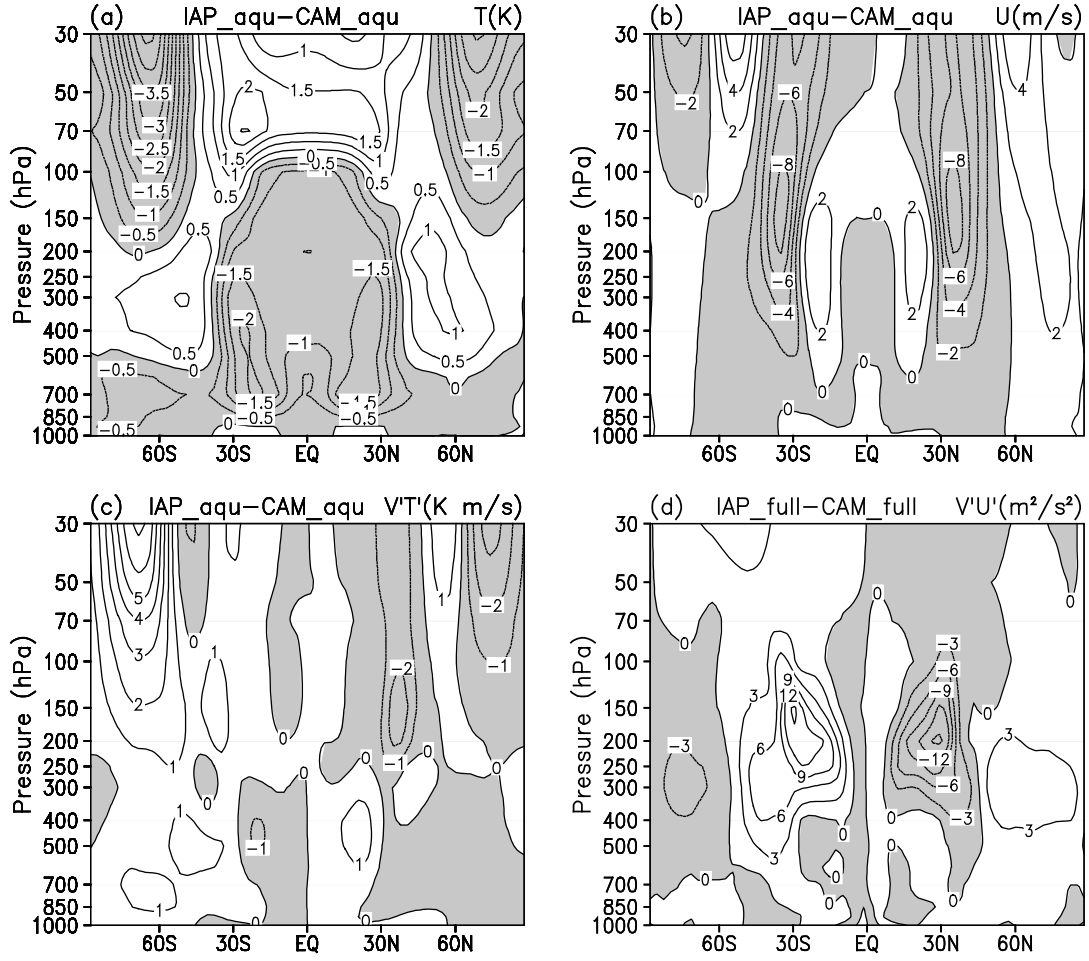


Fig. 9. The difference of zonally averaged annual mean between IAP and CAM from aqua planet tests: (a) temperature; (b) zonal wind; (c) transient eddy heat flux; (d) transient eddy momentum flux. Contour intervals are 0.5 K in (a), 2 m s<sup>-1</sup> in (b), 1 K m s<sup>-1</sup> in (c), 3 m<sup>2</sup> s<sup>-2</sup> in (d), and negative values are shaded.

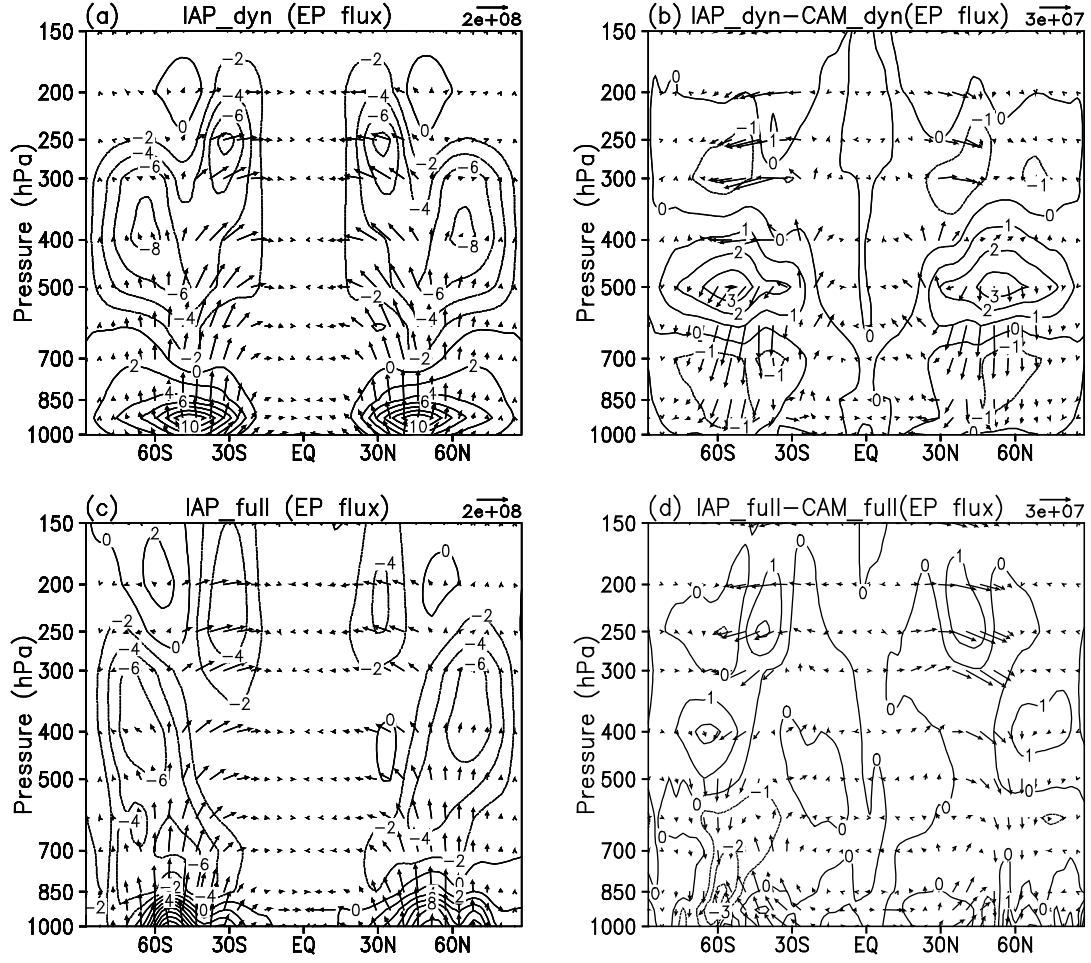


Fig. 10. Vector EP flux and its divergence from the Held-Suarez tests with the (a) IAP and (b) differences between IAP and CAM dynamical cores (IAP - CAM), and from climate simulations from (c) IAP AGCM4.0 and (d) differences between IAP AGCM4.0 and CAM3.1 (IAP AGCM4.0 - CAM3.1). Contour intervals are  $2 \text{ m s}^{-1} \text{ day}^{-1}$  in (a) and (c), and  $1 \text{ m s}^{-1} \text{ day}^{-1}$  in (b) and (d). The flux is in the unit of  $\text{kg s}^{-2}$ . The vertical component of the flux is multiplied by a factor of 100 to make proper vector plots.

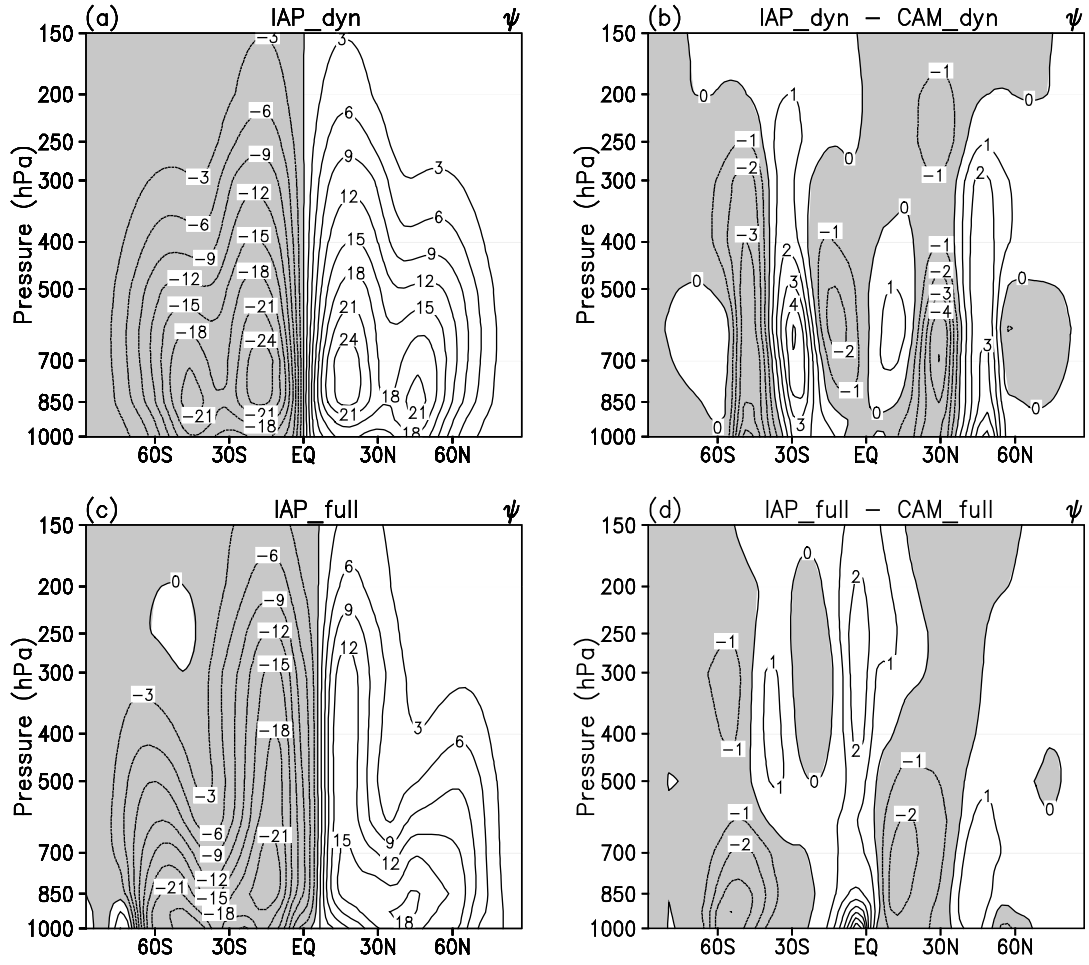
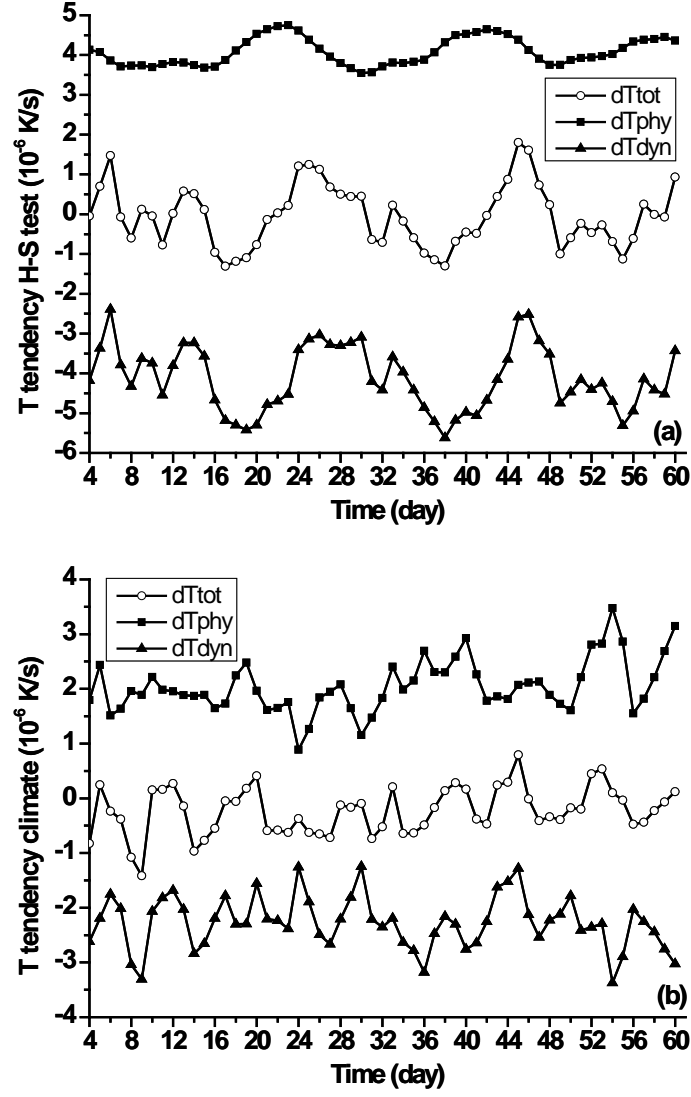


Fig. 11. Same as Fig. 10, but for meridional stream function of residual circulation. Contour intervals are  $3 \times 10^2 \text{ kg m}^{-1} \text{ s}^{-1}$  in (a) and (c), and  $1 \times 10^2 \text{ kg m}^{-1} \text{ s}^{-1}$  in (b) and (d) and negative values are shaded.



1  
2 Fig. 12. Evolution of heating rate from the IAP model in (a) Held-Suarez test and (b)  
3 climate simulation in troposphere (150 hPa – 1000 hPa) at low latitude (30°S - 30°N).  
4 Solid square: diabatic heating rate, solid triangle: adiabatic heating rate, hollow circle:  
5 total heating rate. Unit:  $10^{-6} \text{ K s}^{-1}$   
6

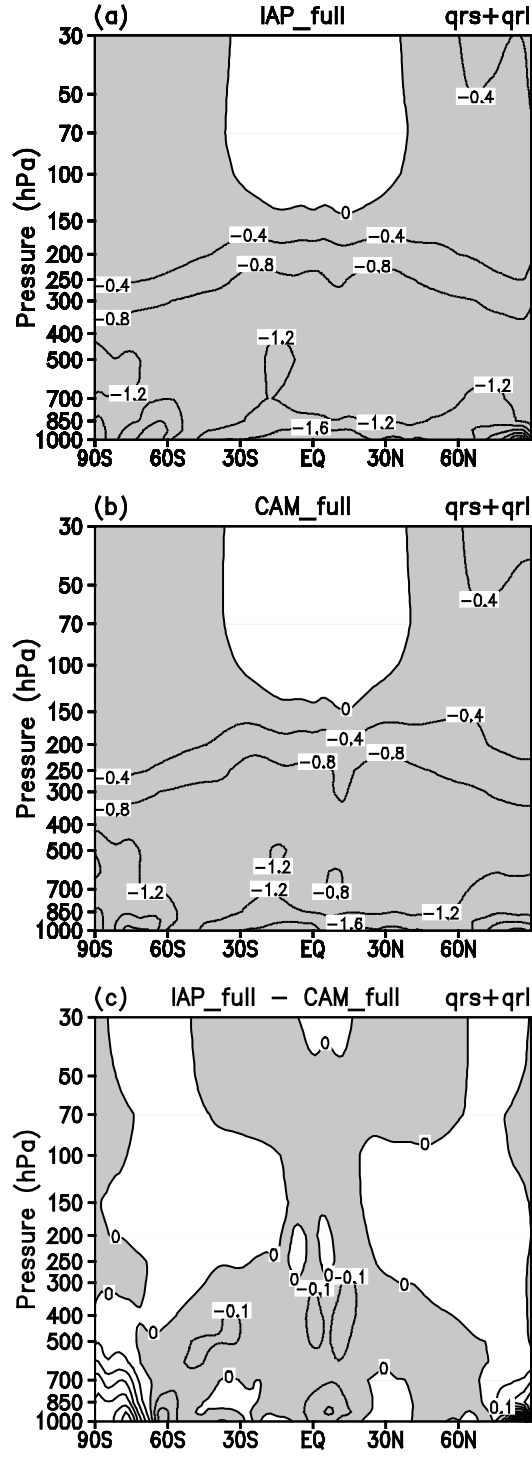


Fig. 13. Zonally averaged annual mean radiative diabatic heating rate from (a) IAP and (b) CAM simulations, and (c) their difference (IAP - CAM). Contour intervals are 0.4 K day<sup>-1</sup> in (a) and (b), 0.1 K day<sup>-1</sup> in (c) and negative values are shaded.

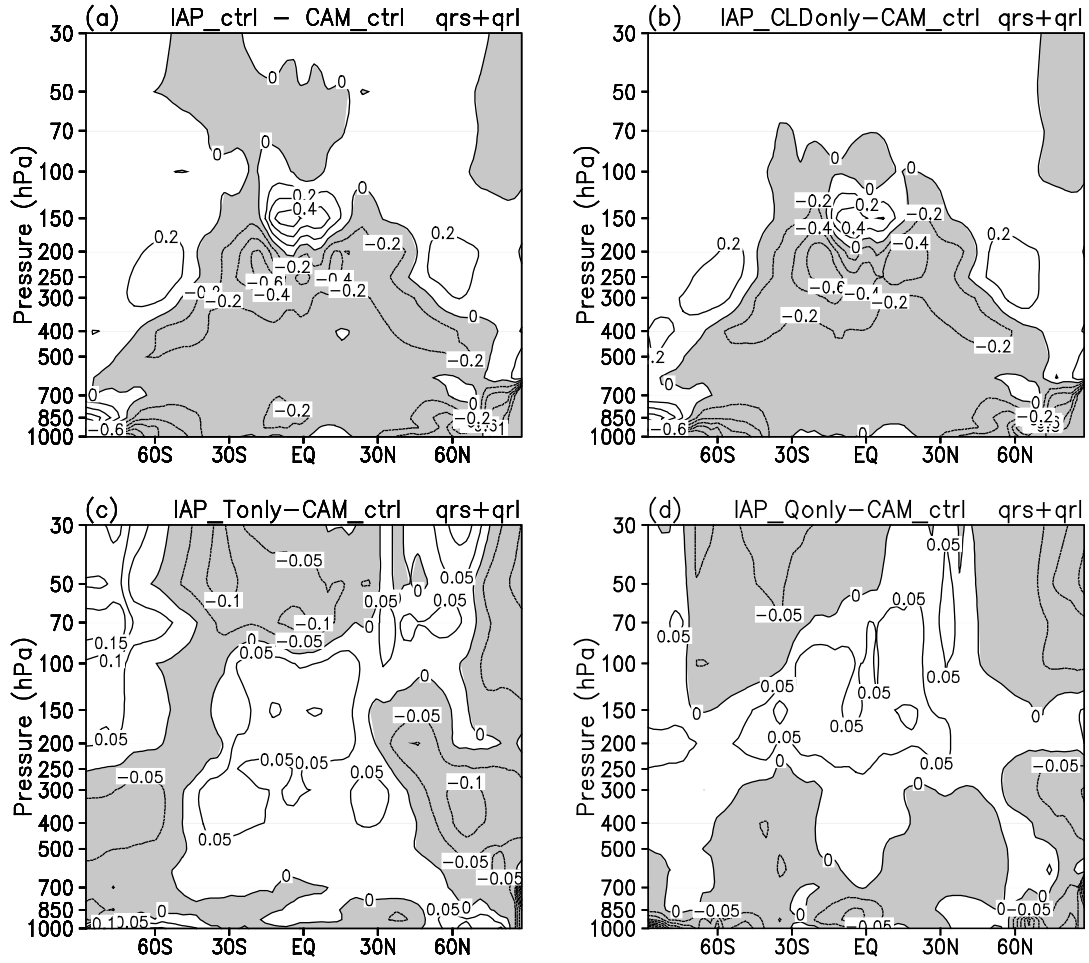


Fig. 14. Differences of radiative diabatic heating rate from the sensitive experiments:  
(a) IAP\_ctrl - CAM\_ctrl, (b) IAP\_CLDonly - CAM\_ctrl, (c) IAP\_Tonly - CAM\_ctrl,  
(d) IAP\_Qonly - CAM\_ctrl. Contour intervals are 0.2 K day<sup>-1</sup> in (a) and (b), 0.05 K  
day<sup>-1</sup> in (c) and (d), and negative values are shaded.

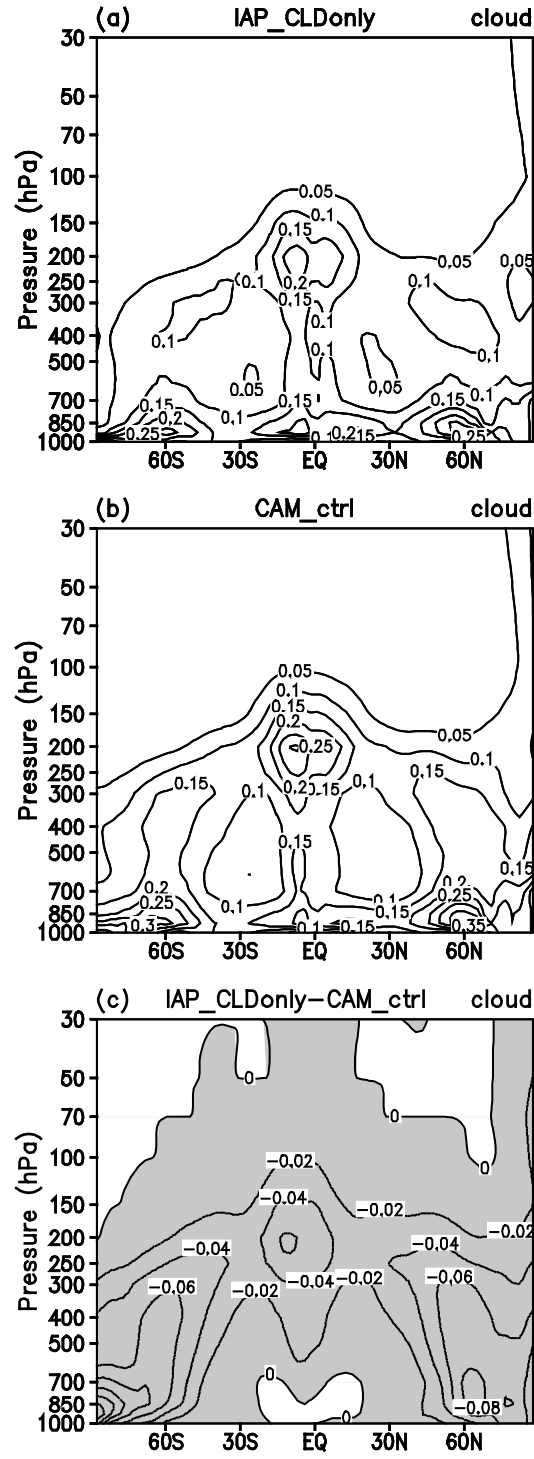


Fig. 15. Cloud fraction used in experiment (a) IAP\_CLDonly and (b) CAM\_ctrl, and (c) their difference (IAP\_CLDonly - CAM\_ctrl). Contour values are 0.05 in (a) and (b), 0.02 in (c) and negative values are shaded.